Multiple polarization mechanisms across the ferroelectric phase transition of the tetragonal tungsten-bronze $Sr_{0.35}Ba_{0.69}Nb_2O_{6.04}$

E. Buixaderas,[1,*] M. Kempa,[1] V. Bovtun,[1] C. Kadlec,[1] M. Savinov,[1] F. Borodavka,[1] P. Vaněk,[1] G. Steciuk,[2] L. Palatinus,[2] and J. Dec[3]

[1]*Institute of Physics, Department of Dielectrics, Czech Academy of Sciences, Na Slovance 2, 18221 Prague, Czech Republic*

[2]*Institute of Physics, Department of Structure Analysis, Czech Academy of Sciences, Cukrovarnická 10, 16200 Prague, Czech Republic*

[3]*Institute of Materials Science, University of Silesia, Pl-40-007 Katowice, Poland*

(Received 27 August 2018; published 26 December 2018)

The broadband dielectric response of the uniaxial ferroelectric strontium barium niobate with 35% Sr has been studied from 1 kHz to 30 THz along the polar *c* axis using high-frequency and low-frequency dielectric spectroscopies, time-domain terahertz spectroscopy, and far-infrared reflectivity, in the wide temperature interval 20–600 K. The mechanisms that contribute to the ferroelectric phase transition and to the dielectric anomaly in this material are the softening of an anharmonic excitation in the THz range related to cation hopping and the slowing down of a relaxation in the GHz range, which saturates below T_C near 1 MHz. In the ferroelectric phase, a relaxation, related to domain-wall dynamics, appears in the sub-GHz range and hardens on cooling up to 10 GHz. The ferroelectric-paraelectric transition, investigated by electron diffraction, has been assessed to the appearance of a supplementary mirror plane perpendicular to the polar axis.

DOI: 10.1103/PhysRevMaterials.2.124402

I. INTRODUCTION

The tungsten-bronze family presents a great challenge in the understanding of ferroelectricity and relaxor behavior in comparison with ferroelectric perovskites [1]. This family can show hexagonal, orthorhombic, or tetragonal variations. In hexagonal and tetragonal cases, they form uniaxial structures, where one axis is preferential, and they show a strong anisotropy in all their properties [2,3]. In the solid solution $Sr_xBa_{1-x}Nb_2O_6$ (SBN-*X*, with $X = 100x$), the structure is formed by a network of interconnected NbO_6 octahedra forming three types of channels along the *c* axis. The squared channels are occupied by Sr (A1 site), the pentagonal ones by Sr and Ba (A2 site), and the triangular ones are empty [4,5]. As the occupation of the channels is not complete and some sites A1 and A2 are left empty, the structure is *unfilled*. In SBN, an almost perfect tunability from ferroelectric to relaxor behavior is accessible, by changing the Sr content, besides exhibiting exceptional piezoelectric and electro-optical properties [3,6].

Ferroelectric SBN samples have lower Sr content (less than 50%, in general). At high temperature, in the paraelectric phase, they are believed to have the centrosymmetric point group *4/mmm* [7,8], deduced from symmetry considerations. Below T_C, another tetragonal phase appears, with the space group *P4bm* [4], and spontaneous polarization develops along the *c* axis. The detailed scenario of ferroelectricity in tetragonal tungsten-bronzes (TTBs) is still under debate. There are not clear structural data clarifying the atomic positions in the paraelectric phase and, so far, no proper soft phonon mode has been found experimentally; therefore, ferroelectricity has been ascribed to an order-disorder mechanism [9]. However, recent first-principles calculations performed for the end members $SrNb_2O_6$ and $BaNb_2O_6$ showed that ferroelectricity may be a consequence of a cooperative displacement of Nb atoms and that the relaxor properties are rather related to the displacement of the Sr atom inside the pentagonal channels [10]. If this is the case, SBN crystals with low Sr content are the best candidates to unveil the origin of ferroelectricity in this TTB structure.

The ferroelectric sample $Sr_{0.35}Ba_{0.69}Nb_2O_{6.04}$ (SBN-35) has recently been studied by Raman scattering and far-infrared (FIR) reflectivity [11] and it was found that the main phonon anomaly is displayed by the contribution of the polar Nb-O vibrations of A_1 symmetry in the range of 180–400 cm^{-1}. This brings evidence that besides the dominating order-disorder character of the ferroelectric phase transition in SBN, phonons play some role on it, which is expected to be revealed in crystals that display strong ferroelectric behavior. Other Raman measurements on SBN-33 and SBN-61 also showed anomalies in the Nb-O stretching vibrations [12,13]; although, again, no clear soft mode at low frequencies was observed. On the contrary, central peaks related to anharmonicity and disorder have been found in this family: neutron scattering in SBN-45 [14] showed a central peak with a half width of ~3 meV (~25 cm^{-1}/0.73 THz) assigned to the anharmonic hopping of Ba/Sr atoms inside the pentagonal channels, and various central peaks discovered by Brillouin scattering [15] at high temperature indicate the thermal switching of the polar nanodomains (PNDs) present in the crystal. Recently it was also found that the reduction of SBN-61 crystals leads to the formation of defects and enhancement of a broad central peak contribution in the Raman spectrum [16]. At similar frequencies, in the THz range, a strong overdamped mode related to anharmonic hopping of cations was found below phonons in several SBN compositions. The broadband dielectric behavior

*buixader@fzu.cz

(from 100 Hz to 67 THz) including the far-infrared (far-IR) reflectivity spectrum of the relaxor samples SBN-61 [9] and SBN-81 [17] was reported by us and we discovered that a soft central mode in the THz range is present in both cases, as well as relaxations related to PNDs below the GHz range.

All these data support the existence of a complex mechanism leading to the ferroelectric phase transition in TTBs, involving polar regions of different correlation lengths, which needs to be addressed in a broadband spectroscopic approach. As there are only a few structural results in ferroelectric SBN crystals at high enough temperatures to investigate the real structure of the paraelectric phase, the structural origin of the phase transition should be complementarily explored as well. According to our knowledge, results of dielectric measurements at frequencies below phonons in the THz and microwave (MW) range were not published for the nonrelaxor SBN crystals. Therefore, the aim of this paper is to explore the structural basis of the ferroelectric phase transition in the ferroelectric SBN-35 single crystal and to investigate its high-frequency dielectric response to find the polar mechanisms that contribute to the dielectric anomaly and assess the origin of ferroelectricity.

II. EXPERIMENT

The SBN-35 single crystal was grown by the Czochralski method. Details about the growth can be found elsewhere [18]. Samples with different geometries were cut from a big bulk crystal to fit the experimental requirements of several techniques as follows:

For transmission electron microscopy (TEM) investigations, a piece of SBN-35 crystal was crushed in ethanol. A drop of the suspension was deposited and dried on a copper grid with a thin film of holey amorphous carbon. Electron-diffraction investigations, including precession electron-diffraction tomography (PEDT), were performed on a Philips CM120 electron transmission microscope (Vacc = 120 kV, LaB6) with the precession device Nanomegas Digistar and a side-mounted CCD camera Olympus Veleta with a 14 bit dynamic range. PEDT data of nonoriented patterns were recorded at several temperatures from 100 to 625 K on one thin crystal with the precession angle set to 1.0 degree, with 1 degree tilt step for the goniometer. PEDT data were analyzed using the computer programs PETS [19] and JANA2006 [20].

Differential scanning calorimetry (DSC) was carried out with a PerkinElmer Pyris Diamond DSC calorimeter. The sample (of ∼33 mg) was heated from room temperature to 500 K at a rate of 10 K min^{-1} and cooled at the same rate, after holding at this temperature for one minute. Further measurements at 5, 2, and 1 K min^{-1} were also performed. The calorimetric sample holder was purged by nitrogen at 20 ml min^{-1}. The PerkinElmer PYRIS software, version 13.1.1, was used for control and evaluation. Three measurements of the same crystal were performed to check reproducibility.

The time-domain transmission THz spectroscopy (TDTTS) measurements were performed on a thin polished plane-parallel sample (∼4 × 4 × 0.05 mm^3) with orientation (100) in the temperature range of 10–800 K, using a polarized electromagnetic field parallel to the *c* axis to measure the $\boldsymbol{E}\|\boldsymbol{c}$ spectra. A custom-made time-domain THz transmission spectrometer was used to obtain the complex dielectric response from 10 to 90 cm^{-1} (0.3–3 THz) with a resolution of 0.5 cm^{-1}. An Optistat CF cryostat with Mylar windows was used for measurements down to 10 K. An adapted commercial high-temperature cell Specac P/N 5850 without windows was used to heat the sample up to 800 K.

Far-infrared (IR) reflectivity spectra were acquired using a Fourier spectrometer Bruker IFS 113v with pyroelectric detectors as well as a He-cooled (1.5 K) Si bolometer. Further details are explained in Ref. [11].

The dielectric measurements in the high-frequency (HF) range (1 MHz–1.8 GHz) were carried out on a cylindrical

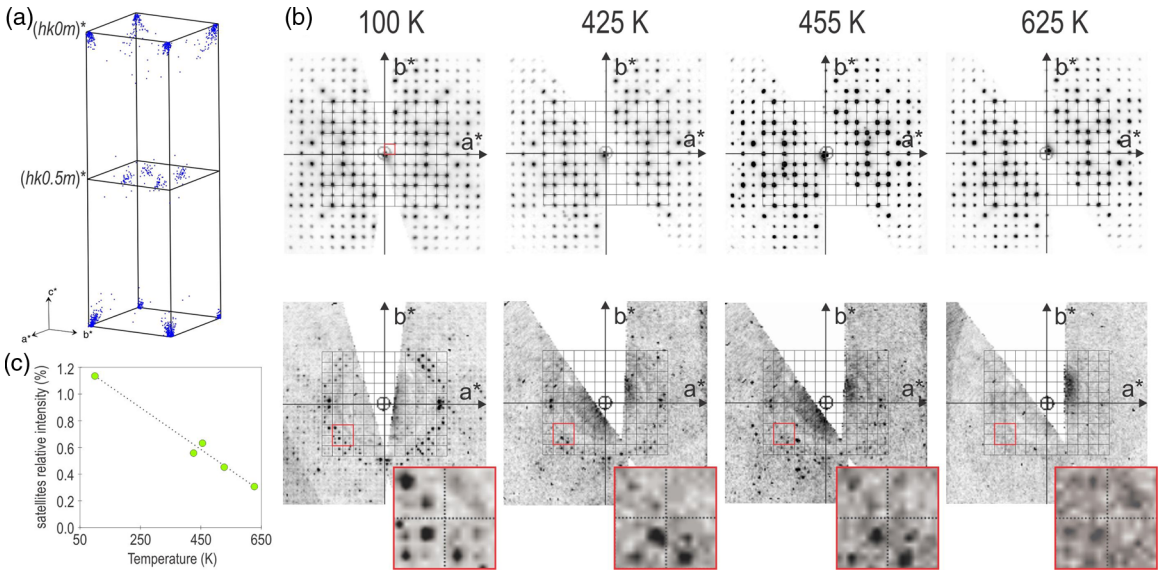

FIG. 1. (a) Reflections projected in one unit cell with the tetragonal settings. (b) (hk0m)* and (hk0.5m)* sections from PEDT recorded on one SBN-35 crystal at several temperatures in the tetragonal settings. Insets in red show the gradual disappearance of the satellites on heating and are illustrated on the (c) plot representing the relative average intensity of the satellites over the main reflections at several temperatures.

TABLE I. Atomic parameters of SBN-35 at 625 K.

	Positional parameters					ADP harmonic parameters			
Atom	Occup.	x/a	y/b	z/c	Wyckoff.	U11	U22	U33	U12
Sr1	0.6426	0	0	0.5	2*b*	0.0122(9)	0.0122(9)	0.017(2)	0
Ba/Sr2	0.812/0.116	0.67280(8)	0.17280(8)	0.5	4*h*	0.0474(6)	0.0474(6)	0.0274(10)	−0.0188(7)
Nb1	1	0.5	0	0	2*d*	0.0156(6)	0.0156(6)	0.0320(15)	−0.0012(8)
Nb2	1	0.21110(8)	0.07355(8)	0	8*i*	0.0165(5)	0.0148(5)	0.0222(7)	0.0020(4)
O3	1	0.5	0	0.5	2*c*	0.046(3)	0.046(3)	0.012(5)	−0.004(4)
O2	1	0.2066(3)	0.0761(3)	0.5	8*j*	0.030(2)	0.050(3)	0.011(2)	−0.0032(19)
O1	1	0.3438(3)	−0.0058(3)	0	8*i*	0.0105(16)	0.0213(18)	0.044(3)	0.0036(15)
O4	1	0.0689(3)	0.1409(3)	0	8*i*	0.0114(17)	0.023(2)	0.045(3)	0.0070(14)
O5	1	0.2830(3)	0.2170(3)	0	8*i*	0.0158(14)	0.0158(14)	0.023(3)	0.0007(18)

sample (height $h = 3.9$ mm and diameter $d = 0.8$ mm) with the polar c axis along the axis of the cylinder and with Au electrodes sputtered on the bases of the cylinder. A computer-controlled HF dielectric spectrometer equipped with HP 4291B impedance analyzer, a Novocontrol BDS 2100 coaxial sample cell, and a Sigma System M18 temperature chamber (operation range 100–570 K) were used. The impedance of the samples was recorded on cooling at the rate of 1 K/min.

For the low-frequency dielectric measurements (1 kHz–1 MHz), gold electrodes were vacuum deposited onto the faces of a crystal plate ($4.5 \times 5 \times 0.8\,\text{mm}^3$) with orientation (001). A Hewlett-Packard 4192A impedance analyzer was used. The sample was heated and cooled in the temperature range of 20–600 K at a rate of 2 K/min under a probing field of 5 V/cm.

Piezoresponse force microscopy (PFM) was done using an Ntegra atomic force microscope. The measurements were performed on the same plate as the low-frequency experiment, using a conductive cantilever HQ:NSC35/Pt in a contact mode. The frequency of the alternating voltage was set to 23.5 kHz and the amplitude up to 6 V. The vertical and lateral PFM signals were amplified and analyzed with an external SR830 DSP Lock-In Amplifier.

III. RESULTS AND EVALUATION

A. Electron-diffraction tomography investigation

Most of the structural studies in SBN single crystals were performed at room temperature. According to our knowledge, the diffraction experiments reported in the literature did not show data far above the phase transition, just up to 500 K [21,22]. Although neutron-scattering measurements in SBN-70 up to 773 K showed that there are satellite reflections at incommensurate positions up to that temperature, no atomic positions were published [23]. Therefore, in order to check the real structure of the paraelectric phase in SBN-35, we used the PEDT experiment on a crystallite from the crystal used for the infrared experiment in Ref. [11] up to 625 K. The sample did not show a clear phase transition in the electron-diffraction patterns above T_C; however, at low temperature, it showed satellite reflections located at *hk0.5* planes, in agreement with [26]. Their intensities decrease on heating and almost vanish above 600 K [see Fig. 1(b)]. From the measured data, we can infer that the ferroelectric-paraelectric transition is not associated to the disappearance of the orthorhombic distortion indicated by the presence of faded but visible satellite reflections far after the dielectric transition, but to the apparition of a supplementary mirror plane perpendicular to the c axis. Because the satellite reflections are practically invisible at 625 K, we can consider the tetragonal description a sufficiently good approximation for this temperature [24]. The parent high-temperature structure of SBN-35 can be taken as tetragonal and the parameters for the tetragonal cell at 625 K, in the space group *P4/mbm*, are $a = 12.445(5)$ Å, $c = 3.943(3)$ Å, with $Z = 5$. *P4/mbm* is the only possible tetragonal space group compatible with the observed extinction conditions and the presence of inversion center. This experimental result

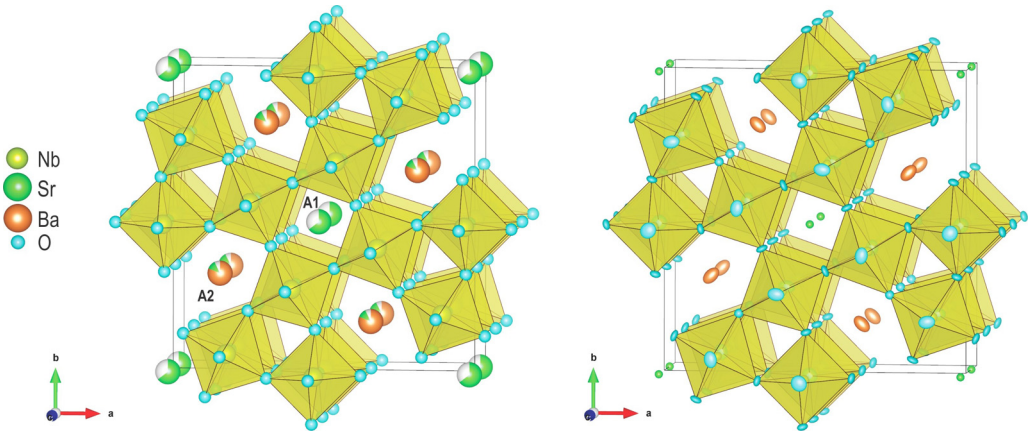

FIG. 2. Refined structure of SBN-35 at 625 K, obtained from the dynamical refinement showing the site occupancies on the left and the anisotropic displacements on the right.

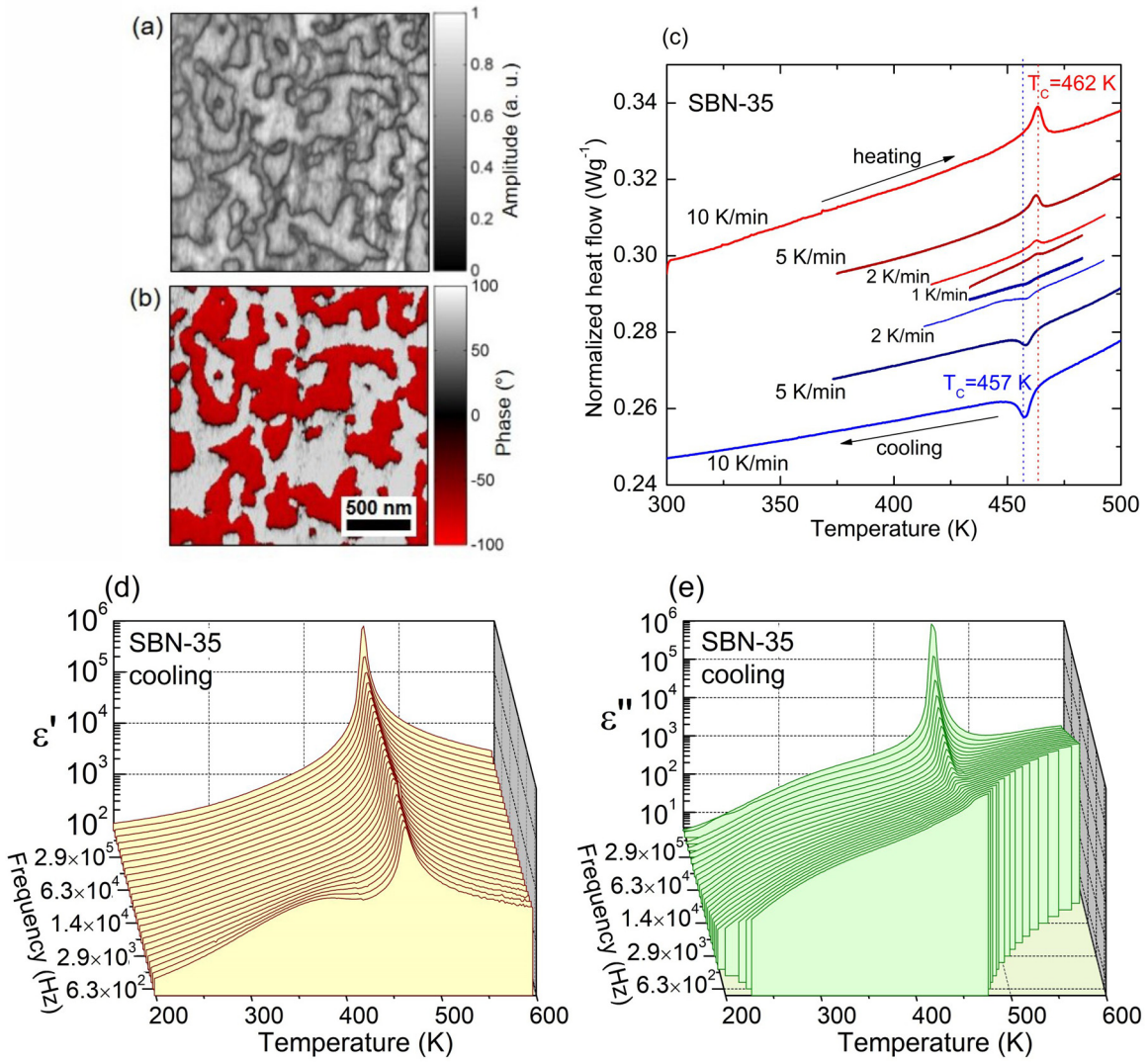

FIG. 3. (a), (b) PFM images (amplitude and phase) of the SBN-35 single crystal taken at room temperature before the spectroscopic measurements [from 36]. (c) DSC calorimetry curves on heating and cooling. (d), (e) Temperature dependence of dielectric permittivity and losses along the polar axis on cooling.

confirms the symmetry predictions for similar TTBs in the high-symmetry phase [7,8] and settles the space group of the high-temperature paraelectric phase for SBN. Therefore, the phase transition involves a symmetry reduction from the point group 4/*mmm* to the point group 4*mm* corresponding to the species 49 and it is fully ferroelectric according to [25]. In Table I, we show the positional parameters for each atom and also the displacement parameters arising from the dynamical refinement ($N_{obs}/N_{all} = 3364/4095$ $R_{obs} = 8.19\%$, $wR_{obs} = 9.23\%$, and 40 refined structural parameters) [26,27]. These parameters were used to plot the structure in Fig. 2.

B. Piezoresponse force microscopy, calorimetric and dielectric characterization

The SBN-35 crystal was checked by the PFM technique in order to see the real domain structure and corroborate its nonrelaxor nature. In Figs. 3(a) and 3(b), we see the amplitude and phase images taken at room temperature in vertical mode, in a 0.8-mm-thick sample with the *c* axis perpendicular to the image plane, showing an irregular distribution of domains forming an entangled pattern. Domain boundaries are seen in the amplitude image [Fig. 3(a)] and they are strongly twisted in a fractal-like manner. The domain walls are also seen, but due to experimental limitations and the width of the tip, it is not possible to obtain a real estimation of their width, although it is probably less than 50 nm. The gray and red colors in Fig. 3(b) correspond to domains with the spontaneous polarization oriented up and down along the polar axis, and they have a distribution of sizes from 100 to about 800 nm. These domains have a shape similar to the one found in SBN-40 [28].

Calorimetric measurements of SBN-35 were performed on the same plate on heating and cooling at several rates, from 1 to 10 K min^{-1}. Results normalized by the mass (∼33 g) are presented in Fig. 3(c). For each rate, after heating, the

TABLE II. Site group analysis of SBN for an ideally filled structure with (a) averaged Ba/Sr atom and (b) individual Sr and Ba atoms. Polar modes along the ferroelectric axis are in bold.

Averaged Ba/Sr atom		Individual Ba and Sr atoms	
Paraelectric phase P4/*mbm* $Z = 5$	Ferroelectric phase *P*4*bm* $Z = 5$	Paraelectric phase P4/*mbm* $Z = 5$	Ferroelectric phase P4*bm* $Z = 5$
46 atoms: site 2*b*: 1 Sr site 4*h*: **1 Ba/Sr** + 1 O sites 2*cd*: 1 Nb + 1 O sites 8*i,j*: 1 Nb + 3 O	46 atoms: site 2*a*: 1 Sr site 4*c*: **1 Ba/Sr** + 1 O site 2*b*: 1 Nb + 1 O site 8*d*: 1 Nb + 3 O	50 atoms: site 2*b*: 1 Sr site 4*h*: **1 Ba** + **1 Sr** + 1 O sites 2*cd*: 1 Nb + 1 O sites 8*i,j*: 1 Nb + 3 O	50 atoms: site 2*a*: 1 Sr site 4*c*: **1 Ba** + **1 Sr** + 1 O site 2*b*: 1 Nb + 1 O site 8*d*: 1 Nb + 3 O
10 $A_{1g}(aa\,bb\,cc)$ **9 A_{2u}(c)** 10 $E_g(ac\,bc)$ − doublet 26 E_u(a, b) − doublet 10 $B_{1g}(aa\,bb)$ 10 $B_{2g}(ab)$ 4 $B_{2u}(-)$ 5 $A_{1u}(-)$ 10 $A_{2g}(-)$ 8 $B_{1u}(-)$	**19 A_1(c, *aa bb cc*)** 36 *E*(a b, *ac bc*) − doublet 14 $B_1(-, aa\,bb)$ 18 $B_2(-, ab)$ 15 $A_2(-)$	11 $A_{1g}(aa\,bb\,cc)$ **10 A_{2u}(c)** 11 $E_g(ac\,bc)$ 28 E_u(a, b) 11 $B_{1g}(aa\,bb)$ 11 $B_{2g}(ab)$ 4 $B_{2u}(-)$ 5 $A_{1u}(-)$ 11 $A_{2g}(-)$ 9 $B_{1u}(-)$	**21 A_1(c, *aa bb cc*)** 39 *E*(a b, *ac bc*) 15 $B_1(-, aa\,bb)$ 20 $B_2(-, ab)$ 16 $A_2(-)$
138 modes	138 modes	150 modes	150 modes:
18 external: $A_{1u} + \mathbf{2}\,A_{2u} + 4E_u$ $+B_{1u} + A_{1g} + A_{2g}$ $+B_{1g} + B_{2g} + E_g$	18 external: $\mathbf{3}\,A_1 + 5\,E + B_1 + 2\,B_2$ $+2\,A_2$	30 external $A_{1u} + \mathbf{3}\,A_{2u} + 6\,E_u + 2\,B_{1u}$ $+2\,A_{1g} + 2\,A_{2g} + 2\,B_{1g}$ $+2\,B_{2g} + 2\,E_g$	30 external: $\mathbf{5}\,A_1 + 8\,E + 2\,B_1 + 4\,B_2 + 3\,A_2$
120 internal NbO_6 : $\mathbf{4}\,A_{1u} + 7\,A_{2u} + 22\,E_u + 7\,B_{1u}$ $+4\,B_{2u} + 9\,A_{1g} + 9\,A_{2g}$ $+9\,B_{1g} + 9\,B_{2g} + 9\,E_g$	120 internal NbO_6 : $\mathbf{16}\,A_1 + 31\,E + 13\,B_1$ $+16\,B_2 + 13\,A_2$	120 internal NbO_6 : $\mathbf{4}\,A_{1u} + 7\,A_{2u} + 22\,E_u + 7\,B_{1u}$ $+4\,B_{2u} + 9\,A_{1g} + 9\,A_{2g}$ $+9\,B_{1g} + 9\,B_{2g} + 9\,E_g$	120 internal NbO_6 : $\mathbf{16}\,A_1 + 31\,E + 13\,B_1$ $+16\,B_2 + 13\,A_2$

sample was held one minute at the maximum temperature and then cooled down at the same rate. The ferroelectric phase transition is well detected at all rates: heating and cooling curves show clear peaks and reveal a small thermal hysteresis of about 5 degrees. The wide shape of the peak does not change with the rate; therefore it is intrinsic to the nature of the transition, which seems to be of weak first order. The calculated enthalpy has values near $0.4\,J\,g^{-1}$ and the temperature of the phase transition on cooling is $T_C \sim 457\,K$.

Low-frequency dielectric measurements taken afterwards on this plate confirmed this picture. In Figs. 3(d) and 3(e), the real and imaginary parts of the complex permittivity are depicted, showing again a sharp peak at the phase transition. The maxima of $\varepsilon'(T)$ and $\varepsilon''(T)$ are located at $T_C \sim 460\,K$.

C. Far-IR and THz measurements

The results of the site group analysis of the lattice vibrations for SBN-35 are summarized in Table II, for the case of an averaged Ba/Sr atom in the pentagonal site, and also for the case in which Ba and Sr are taken as separated atoms. In the case of the averaged atom, there are 46 atoms in the unit cell and the polar vibrations active along the *c* axis are $9A_{2u}(c;-)$ in the paraelectric phase, and $19\,A_1(c; a^2 + b^2, c^2)$ in the ferroelectric phase. IR and Raman activities are shown in parentheses. However, taking into account that there are two atoms with quite different masses in the pentagonal channels, Sr and Ba, the number of vibrations coming from these two atoms is doubled. In this case, there are effectively 50 atoms in the unit cell and, in total, we expect $11A_{2u}(c;-)$ modes in the paraelectric phase and $21\,A_1(c; a^2 + b^2, c^2)$ in the ferroelectric phase (see Table II). Out of them, one A_{2u} and one A_1 are acoustic phonons, and three A_{2u} modes and five A_1 modes belong to the external vibrations—due to Ba and Sr vibrations—corresponding to phonons with frequencies below $\sim 180\,cm^{-1}$ [11,29]. The other higher-frequency modes are due to Nb-O stretching and bending vibrations in the octahedral network, as is known for SBN and other TTBs [30].

The far-IR reflectivity spectra of vibrations along the polar axis, showing modes of A_{2u}/A_1 symmetry, were published in Ref. [11]; however, without data collected by TDTTS experiment and without their proper normalization. Therefore in Fig. 4(a), we show the far-IR spectra normalized with the points measured in the THz range and the corresponding fits at selected temperatures. These reflectivity spectra were fitted with the generalized oscillator model of the dielectric function [31], as explained in [11,17]. Below phonons, there is an extra mode to fit the THz data and, in addition, at lower frequencies another contribution was taken into account to obtain the values of the permittivity in the MHz–GHz range. This model is called fit 1:

$$\hat{\varepsilon}(\nu) = \varepsilon'(\nu) - i\varepsilon''(\nu) = \varepsilon_\infty \prod_{i=1}^{n} \frac{\nu_{LOi}^2 - \nu_2 + i\nu\gamma_{LOi}}{\nu_{TOi}^2 - \nu^2 + i\nu\gamma_{TOi}}, \quad (1)$$

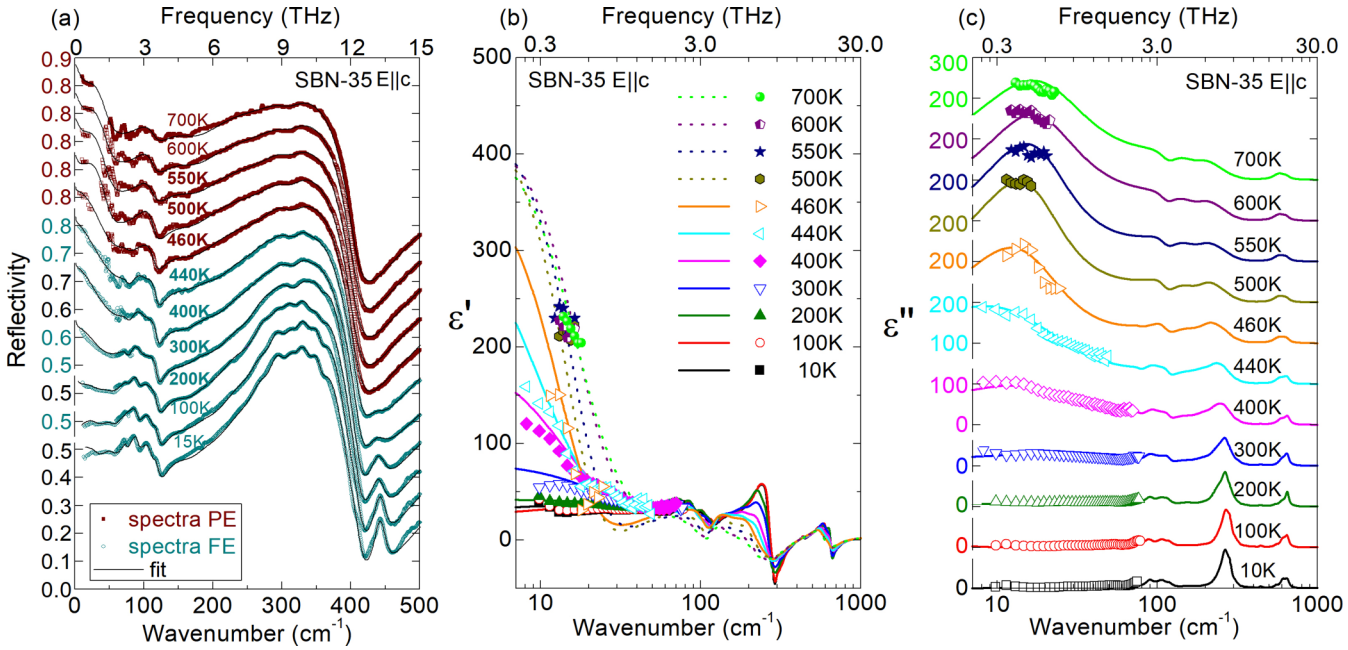

FIG. 4. (a) IR reflectivity spectra of SBN-35 (dotted) together with their fits (lines) at several temperatures for the $E\|c$ polarization, including the experimental TDTTS data in the THz range. (b), (c) Permittivity and dielectric loss functions of SBN-35 obtained from the FIR fit of the reflectivity at different temperatures, together with the points measured in the TDTTS experiment.

where ε_∞ is the permittivity at frequencies much higher than phonon frequencies, ν_{TOi} and ν_{LOi} are the transverse and longitudinal frequencies of the ith phonon mode, and γ_{TOi} and γ_{LOi} are their respective damping constants. The dielectric permittivity and losses calculated from these fits are presented together with the experimental TDTTS points in Figs. 4(b) and 4(c), at selected temperatures.

In the paraelectric phase, eight A_{2u} modes were fitted (three external modes plus five internal ones) and an extra overdamped low-frequency mode in the THz range. The theoretical group analysis provides a result of $9A_{2u}$ optical modes, after subtracting the acoustic one. Probably there is one more mode inside the highest-frequency band (not measured above 600 cm^{-1} because of the frequency cut of the windows in the cryostat) as seen in [11]. In the ferroelectric phase, at the lowest temperature, 20 A_1 were fitted (5 external modes and 15 internal modes) plus a low-frequency excitation in the THz range, in agreement with the theoretical prediction. Phonon frequencies above 50 cm^{-1} show no important anomalies on cooling from 700 K, as in SBN-61; but below T_C, new phonons appear. An overdamped feature, the central mode (CM), shows a pronounced softening towards T_C, and it is, at least partially, responsible for the phase transition.

Table III presents the list of the phonon parameters (transverse frequency ν_T, transverse damping γ_T, and dielectric strength $\Delta\varepsilon$) calculated from the combined THz–far-IR fit, at three temperatures: one in the paraelectric phase and two in the ferroelectric one. In addition, it shows relaxations present below phonons down to the kHz range, which were used in another fit explained in Sec. III D. The external modes due to Sr and Ba cations in the channels are located in the lower part of the reflectivity spectra (below about 180 cm^{-1}). The five A_1 external modes expected in the ferroelectric phase should stem from the three A_{2u} modes in the paraelectric phase. A closer look to the reflectivity spectra in Fig. 4(a) shows that this is the case. Also, in Table III, there are three modes at 500 K with frequencies $\nu_T \sim 75$, 113, and 152 cm^{-1}, and at 100 K, we found five modes with $\nu_T \sim 75$, 90, 111, 116, and 162 cm^{-1}. The dielectric strength of the CM changes from 300 at 500 K to ~1 at 100 K, and its frequency rises from ~12 to 35 cm^{-1}. This excitation has the character of an anharmonic phonon and it corresponds, probably, to some rambling motion of the cations inside the channels around their crystallographic sites. Below 100 K, this mode splits into two weaker contributions (frequencies $\nu \sim 35$ and $\nu \sim 59$ cm^{-1}); this could be due to the presence of two different cations (Sr/Ba) in the same channels.

The phonon contribution to the permittivity along the polar axis is rather low ($\varepsilon'_c \sim 40$), as in other TTB materials [32], but the CM enhances dramatically the permittivity $\varepsilon'(\nu)$ values in the THz range, near 10 cm^{-1}, at high temperatures [see Fig. 4(b)]. On cooling, the CM dielectric strength almost vanishes and the permittivity at THz frequencies practically coincides with the phonon contribution. In Fig. 4(c), the dielectric loss spectra are displayed at different temperatures. Each peak or maximum corresponds to a phonon mode. On cooling, all phonons are better distinguished and, in the THz range and at high temperatures, the intense CM is seen as a broad peak, which, below T_C, gradually weakens and shifts to higher frequencies.

D. High-frequency dielectric measurements

The HF dielectric data obtained by the coaxial technique are shown in Fig. 5. Figure 5(a) shows the temperature dependence of permittivity and losses for selected frequencies. The frequency dependence of the permittivity and dielectric loss for different temperatures is depicted in Figs. 5(b) and 5(c),

TABLE III. Parameters of the relaxations used in fit 2 [Eq. (2)] and the low-frequency polar phonons of SBN-35 [fit 1, Eq. (1)] along the polar axis in paraelectric and ferroelectric phases (ν_0 in Hz, ν_T and γ_T in cm^{-1}). Phonons above 160 cm^{-1} are the same as in Ref. [11].

	SBN-35 $E\|\|c$ A_1/A_{2u} modes								
	Ferroelectric phase (100 K)			Ferroelectric phase (400 K)			Paraelectric phase (500 K)		
	ν_0 (Hz)	α	$\Delta\varepsilon$	ν_0 (Hz)	α	$\Delta\varepsilon$	ν_0 (Hz)	α	$\Delta\varepsilon$
Relaxations	6.7×10^5	0.55	8	6.0×10^6	0.36	450	8.8×10^7	0.2	6000
	7.6×10^9	0.47	4	1.7×10^9	0.35	170			
	ν_T (cm^{-1})	γ_T (cm^{-1})	$\Delta\varepsilon$	ν_T (cm^{-1})	γ_T (cm^{-1})	$\Delta\varepsilon$	ν_T (cm^{-1})	γ_T (cm^{-1})	$\Delta\varepsilon$
CM	*35.3*	*24*	*0.9*	*26.8*	*60*	*118*	*11.9*	*27.0*	*300*
	59.0	*25*	*0.2*						
External modes	75.4	7.3	0.1	77.0	14.4	0.3	75.0	66.5	2.7
	90.2	14.1	2.0	91.6	21.9	1.9			
	110.7	26.8	4.5						
	116.0	11.3	1.4	118.1	18.3	1.1	113.0	31.0	3.4
	161.7	89.3	5.8	160.0	100.7	6.4	152.0	105.0	17.2
Internal modes	185.8	57.4	3.1	186.7	62.8	6.9			
	236.4	57.9	5.7	231.6	60.0	4.9	209.0	102.0	20.6
	265.6	31.2	1.4	266.2	49.5	1.1	291.0	91.0	0.1
	287.9	23.8	1.0	292.0	57.5	2.1	313.0	48.0	0.3
	310.8	27.6	1.1	323.0	35.4	0.4			
	320.4	22.9	0.5						
	345.7	27.3	0.3	345.5	37.5	0.2			
	357.0	23.6	0.1	357.1	45.1	0.06			
	404.8	54.7	0.1	404.8	65.0	0.05			
	441.0	18.5	0.1	437.1	37.1	0.1			
	551.8	36.1	0.3						
	597.5	52.7	1.0	584.3	73.9	1.2	569.8	106.2	2.3
	651.7	50.8	1.7	654.2	65.4	1.7	644.5	82.8	0.9
	735.6	50	0.02	735.5	59.6	0.02			
	775.3	46	0.01	775.3	51.5	0.01			

where we include data from the low-frequency dielectric experiment and also from the TDTTS experiment. Experimental data are marked by symbols and their fits with lines.

The phase transition in SBN-35 is seen as a sharp peak in the dielectric permittivity and loss at $T_C = 460$ K in Fig. 5(a). Maxima do not shift to higher temperatures with increasing frequency; therefore, the crystal shows no traces of relaxor behavior. Nevertheless, a significant HF dielectric dispersion takes place around the sharp $\varepsilon'(T)$ maximum. The HF dielectric dispersion is very broad and, evidently, related to the switching of several polarization mechanisms. In order to understand which mechanism has the leading role in the dielectric response in this frequency range, we fitted the frequency dependence of the measured spectra for different temperatures, in combination with the spectra measured by TDTTS and low-frequency dielectric spectroscopy (fit 2). We used a simple model consisting of a sum of Cole-Cole relaxations for the excitations below phonons, and several Lorentzian functions for the phonons:

$$\hat{\varepsilon}(\nu) = \varepsilon'(\nu) - i\varepsilon''(\nu) = \sum_j \frac{\Delta\varepsilon_{0j}}{1 + (i\nu/\nu_{0j})^{1-\alpha_j}} + \sum \Delta\varepsilon_{\mathrm{ph}} + \varepsilon_\infty, \quad (2)$$

where $\Delta\varepsilon_{0j}$ is the dielectric contribution of the relaxation, ν_{0j} is the mean relaxation frequency, and a_j is a real index between 0 and 1, reflecting the deviation from the pure Debye character ($\alpha = 0$). A sum of Lorentzians $\Sigma\Delta\varepsilon_{\mathrm{ph}}$ was used to simulate the contribution of phonons from the fit in Fig. 4 (their parameters are not relevant for the fit at lower frequencies, just the contribution to permittivity), and the permittivity at much higher frequencies (optical permittivity) was taken as $\varepsilon_\infty \sim 5.3$ ($\varepsilon = n^2$, using the index of refraction $n \sim 2.35$ [33]).

In Fig. 5(b), the permittivity versus frequency is shown for selected temperatures (experimental data and fits). In the THz range, the ε' values increase on heating from the phonons value ~40 at the lowest temperatures, to several hundreds. At lower frequencies, in the MHz–GHz range, the values are much higher, which means that there are further mechanisms contributing to them. The several steps of $\varepsilon'(T)$ and several maxima of $\varepsilon''(T)$ in Figs. 5(b) and 5(c) evidence multiple polarization mechanisms. At high temperatures, the dielectric spectra below phonons can be fitted by Eq. (2) with two excitations in the MHz–THz range (with mean frequencies ν_{THZ} and ν_{01}) and a third one below 1 MHz, which shift towards lower frequencies on cooling. Due to conductivity and thermal history effects in the sample, very noticeable at these frequencies [17], we will not discuss results below the MHz range. On cooling, below 450 K, ν_{THZ} hardens and almost merges to phonons. The other relaxation, ν_{01}, broadens on cooling and splits below 454 K, where another relaxation appears at several GHz, with mean frequency ν_{02};

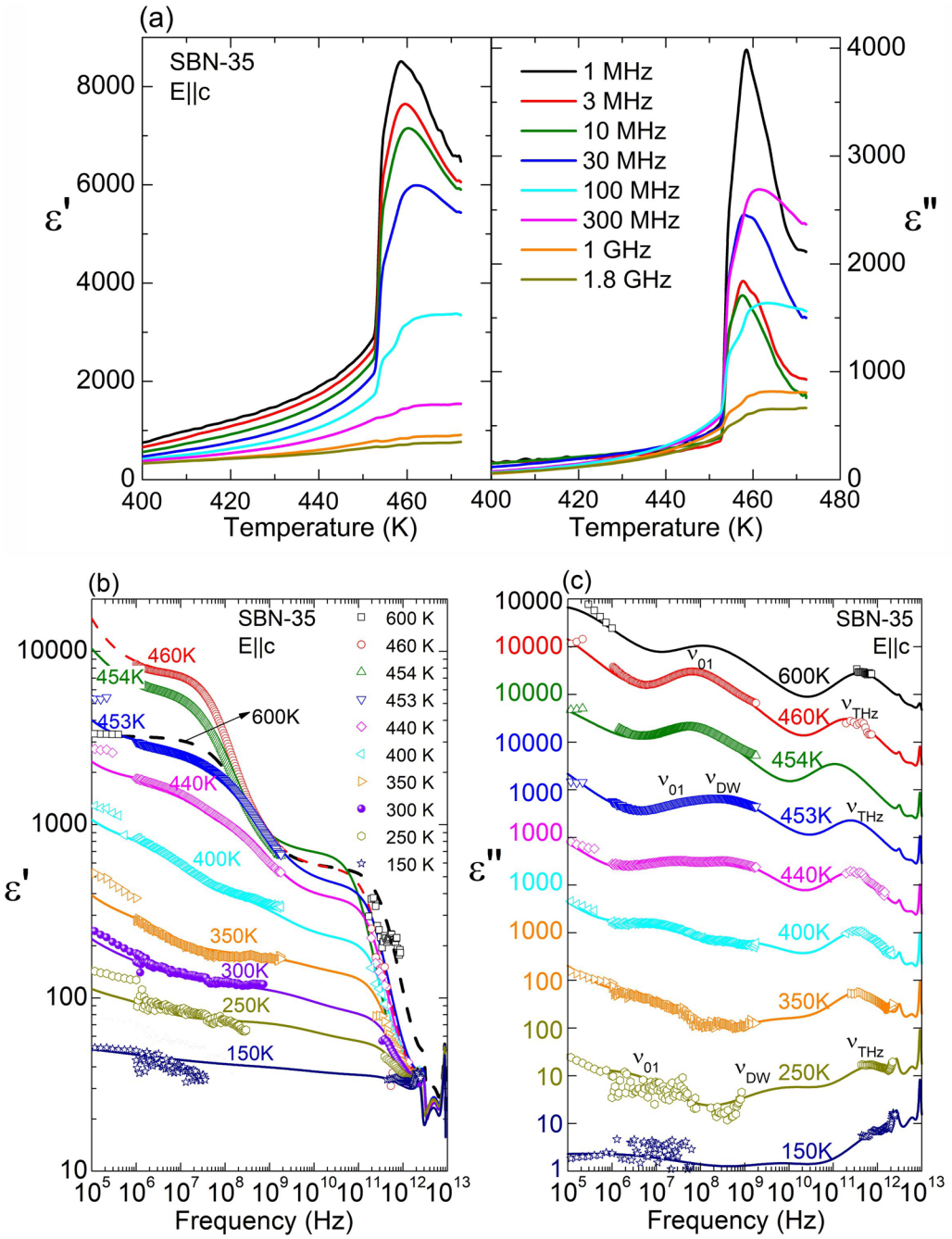

FIG. 5. (a) Permittivity and dielectric loss of SBN-35 vs temperature at high frequencies. Frequency dependences of the (b) permittivity and (c) dielectric loss at different temperatures. Experimental data: open symbols; fits with Eq. (1): lines.

this relaxation will be denoted ν_{DW}, to be consistent with [37]. On further cooling, these two excitations broaden and go away in frequency: ν_{DW} hardens and ν_{01} slows down further.

IV. DISCUSSION

The ferroelectric phase transition in SBN-35 has a first-order ferroelectric character and it shows no signs of relaxor behavior: the peak in permittivity is sharp and does not shift its temperature position with increasing frequency. As it was found in our previous paper [11], a proper soft mode of A_1 symmetry, responsible for the ferroelectric phase transition, was not discovered either in Raman or IR spectroscopy. The fits of the reflectivity including the THz data below 30 cm^{-1} confirm this picture. Although the phase transition involves a structural change, and some phonon parameters display critical-like behavior at T_C (the main anomaly is shown by the polar Nb-O vibrations), the dielectric anomaly is not primarily associated with phonons: its origin lies at lower frequencies.

THz measurements revealed an overdamped CM (ν_{THZ}) with a strong contribution to the permittivity, as found in other TTBs. The origin of this CM has been discussed in other papers [9,17] and, due to its anharmonicity and low frequency, it was excluded from being a proper phonon vibration and

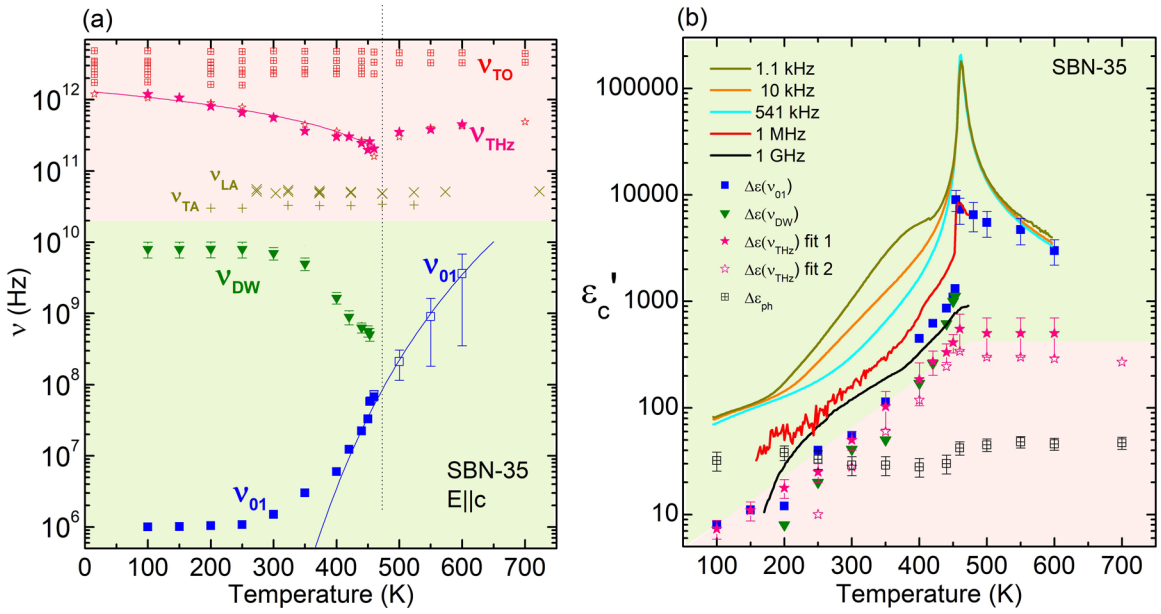

FIG. 6. (a) Temperature dependences of the frequencies of the external polar phonon modes, the central mode ν_{THZ}, the acoustic phonons, and the high-frequency relaxations ν_{DW} and ν_{01}. (b) Permittivity at several frequencies together with dielectric contribution of the different excitations in SBN-35. Note the logarithmic scales.

assigned to hopping or diffusive motion of cations within the channels. Neutron measurements associated it with Ba/Sr motion in the pentagonal channels [14]; however, the picture is still under discussion because hopping of Nb inside the oxygen octahedra could also contribute to this excitation. The most significant feature of the CM is that it behaves like a relaxation, but it shows softening towards the phase transition like a phonon. Its dielectric contribution is about a few hundreds (∼300) near the phase transition. In the relaxor compositions SBN-61 and SBN-81, this CM has even a stronger contribution, about 500 [9,17]. As the ferroelectric composition SBN-35 has less disorder, cationic motions show probably less anharmonicity and contribute less to the permittivity. This agrees with the behavior of the diffuse scattering, which is also less intense in ferroelectric SBN because of the lower anharmonicity [34]. Central peaks or overdamped phonon modes in this frequency region were also reported in Raman and Brillouin spectra [11,15,16]. Interestingly, some authors also reported an extremely broad central peak with FWHM about 300 cm^{-1} in reduced SBN crystals [16] and it was proposed to be related to the dynamics of small polarons, although such contribution is not necessarily visible in the IR spectrum.

The HF dielectric experiment reveals other relaxations below the THz range with temperature-dependent behavior. The most remarkable effects found by this technique are the slowing down of a relaxation in the GHz range and its splitting into two relaxations below the phase transition. In Fig. 6(a), we plot the temperature dependence of the frequencies of the most important excitations found in SBN-35. The contribution of phonons or phononlike excitations are in the upper part, where the external IR phonons are found above 10^{12} Hz. The overdamped CM (depicted by magenta stars) shows an evident softening towards T_{C}. Below them, we plot the frequencies of the acoustic phonons found in the literature for SBN-40 by Brillouin scattering [35], as well as results from our measurements in SBN-35 [36]. The transverse-acoustic (TA) phonon is located near 30 GHz and the longitudinal one (LA) at higher frequency, about 50 GHz. LA shows an anomaly towards T_{C}; however, it is too weak to be observed in the huge frequency scale of Fig. 6(a).

In the frequency range below 10 GHz, excitations of nonphononic origin are revealed. Our dielectric data in the high-frequency range showed that at high temperatures, there is one relaxation (ν_{01}) responsible for the value of the permittivity at in the MHz range. Below T_{C}, ν_{01} splits—clearly seen in the dielectric losses [Fig. 5(c)]—and two distinct relaxations are detected. ν_{01} slows down further, as in other SBN compositions, but the excitation denoted ν_{DW} hardens, which speaks in favor of a different underlying mechanism. This excitation was not found in SBN-61 [9], probably due to lack of the experimental data between the 1–200 GHz. In SBN-81, however, there is an excitation in the 10 GHz range too, which appears below the phase transition, and it was assigned to domain-wall oscillations [17]. The hardening displayed in SBN-35, being a regular ferroelectric material, also resembles the behavior found in PZT, where the domain-wall oscillations display softening and hardening on cooling also in the GHz range [37,38].

The frequency of the CM (ν_{THZ}) was fitted below T_{C} with the renormalized Cochran law for overdamped oscillations,

$$\nu_r = a(T_{\mathrm{C}} - T), \tag{3}$$

where the renormalized frequency of an overdamped oscillator is taken into account, $\nu_{\mathrm{r}} = \nu_{\mathrm{T}}^2/\gamma$. The obtained fitting parameters are $T_{\mathrm{C}} \sim 532$ K and $a = 2.6 \times 10^9\ \mathrm{s}^{-1}\,\mathrm{K}^{-1}$. These parameters are in agreement with those found for SBN-81, where T_{C} extrapolated from the fit was also about 50 degrees higher than the maximum of permittivity at 1 MHz. Above the phase transition, there are not enough experimental data to

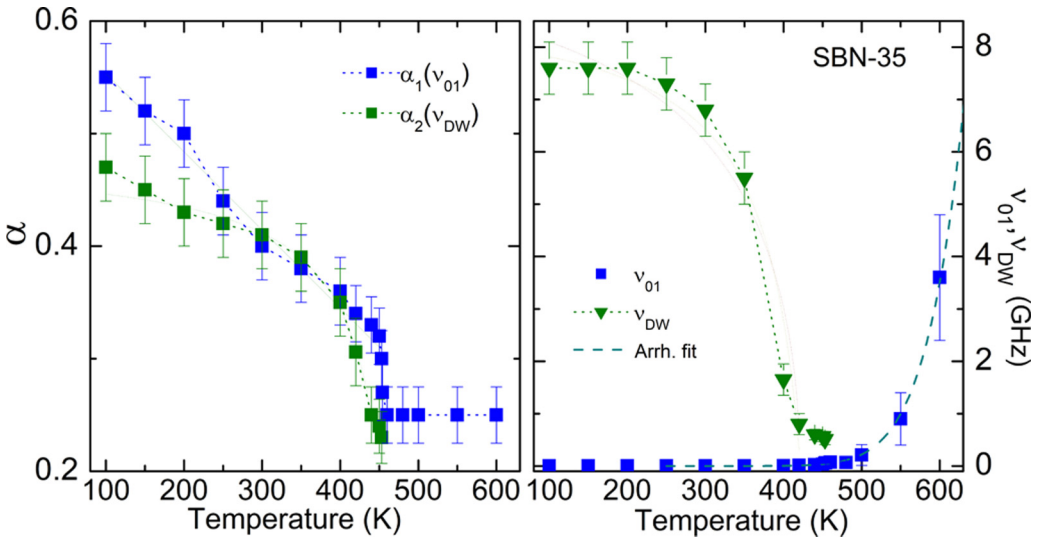

FIG. 7. The α parameters and mean frequencies of the Cole-Cole relaxations used in fit 2, together with the fit with the Arrhenius law for ν_{01}.

perform a reliable fit, but the frequencies increase with heating, which agrees with the overall picture of the ferroelectric phase transition triggered by a high-frequency excitation of nonphononic origin.

The relaxation in the MHz–GHz range, ν_{01}, slows down, following the classical Arrhenius law at high temperatures,

$$\nu = \nu_\infty \exp(-E_a/kT), \tag{4}$$

where ν_∞ is the saturation frequency, E_a is the activation energy, and κ is the Boltzmann constant $k = 8.617 \times 10^{-5}\,\mathrm{eV\,K^{-1}}$. The parameters of the Arrhenius fit are $\nu_\infty = 3580 \pm 1400$ THz and $\mathrm{E}_a/k = 8300 \pm 200\,\mathrm{K}$. The values of the frequency above 460 K are estimations taken from the fit of the THz data and the values of the complex permittivity at 1 MHz from the low-frequency dielectric measurements in Fig. 1(c) because our coaxial setup is not able to measure this relaxation above 480 K. Therefore, the fit above 460 K has to be taken with caution and it is mostly illustrative. Big uncertainty bars were added to Fig. 6(a) with the lower and upper estimations from different fits. Below 460 K, the fit is reliable and the uncertainty in frequencies lies within the point size. At these temperatures, the appearance of the domain-wall relaxation ν_{DW} affects the slowing down of ν_{01} and, below ~300 K, its frequency saturates near 1 MHz while its dielectric strength further reduces on cooling.

The contribution of these excitations to the permittivity is seen in Fig. 6(b), together with measured values at selected frequencies. The maximum of permittivity stays stable near 460 K up to the phonon frequencies, showing the utmost ferroelectric behavior of the crystal. The phonon contribution shows practically no anomaly at T_C, but the contribution from the CM at THz frequencies already shows a maximum at T_C. However, the main origin of the dielectric anomaly in the MHz range is the relaxation ν_{01}. Below 1 MHz, there should be another relaxation to account for the permittivity values at kHz range, as found in SBN-81 [39]. It is worth mentioning that within one degree, from 454 to 453 K, the crystal undergoes a phase transition and the relaxation ν_{01} weakens and is split into two processes [see Fig. 5(c)]. This effect confirms the first-order character of the phase transition. The temperature dependences of the mean relaxation frequencies and α parameters of the two Cole-Cole relaxations used in fit 2 (denoted ν_{01} and ν_{DW}) are shown in Fig. 7. Just below T_C, the two relaxations have small α, around 0.25, and the deviation from the Debye character is not strong. However, on cooling, α increases for both relaxations, indicating their broadening over frequency, although not so pronouncedly as in the relaxor compositions. In Fig. 7, we also show the fit of ν_{01} with the Arrhenius law [Eq. (4)].

The fast excitations found in SBN-35 using both fitting approaches (fit 1 with generalized oscillators at high frequencies, and fit 2 with Cole-Cole relaxations below the THz range) are summarized in Table III. All of them help one to understand the origin of the ferroelectric phase transition in SBN-35. This phase transition is triggered by two excitations: one overdamped CM of anharmonic origin (ν_{THZ}), which softens towards T_C, and a relaxation (ν_{01}), which slows down and then splits below T_C. As found in [40], ν_{01} is related, in the paraelectric phase, with polar fluctuations which develop into ferroelectric domains below T_C. However, in SBN-35, they do not give rise to relaxor behavior and are most probably related with the ordering of Nb atoms inside the oxygen octahedra. The origin of the CM (ν_{THZ}) is still unclear. Due to its high frequency, the associated correlation length must be very small, and therefore it could be caused by the anharmonic rambling motion of the Sr and Ba cations inside the pentagonal channels (A2 sites), which was revealed by their high anisotropic displacements in the electron-diffraction experiment (Fig. 2).

It is clear that all the polar mechanisms found in SBN-35 should be present in other compositions, although the way they influence the development of the ferroelectricity would be different. In SBN-81, we found the same three excitations as in ferroelectric SBN-35, although their individual contributions to permittivity are different. In SBN-61, which is a

mixture of relaxor and ferroelectric with maximal permittivity in the SBN family, the relaxation ν_{01} is so strong that it overwhelms the dielectric spectrum from MHz to THz, showing a permittivity about 15 000 near T_C [9], while SBN-35 shows 8000 and SBN-81 only 4000 at the phase transition [17]. Other intermediate compositions as SBN-70 and SBN-50 should give an insightful hint about how this relaxation evolves with Sr content and how it affects the ferroelectric relaxor behavior.

V. CONCLUSIONS

Multiple mechanisms accountable for the ferroelectric phase transition in a SBN-35 single crystal have been found. Studying the dielectric behavior of SBN-35 from 10^4 to 10^4 Hz by means of various experimental techniques, several excitations with different temperature behavior were revealed. Their individual contributions to the dielectric anomaly can be attributed to different mechanisms:

(i) Phonons, related to cation displacements along the polar axis, contribute to the permittivity with a small amount, $\Delta\varepsilon_{ph} \sim 40$.

(ii) The anharmonic excitation located in the THz range (the CM ν_{THZ}) already makes an important contribution of $\Delta\varepsilon(\nu_{THz}) \sim 300$ near T_C. This CM is presumably caused by the dynamic disorder of Sr and Ba atoms located at the A2 sites in the pentagonal channels, as supported by the high anisotropic displacements found in the electron-diffraction experiment.

(iii) The relaxation in the GHz range, ν_{01}, makes the strongest contribution to the permittivity, $\Delta\varepsilon(\nu_{01}) \sim 10000$ at T_C, and it slows down on cooling. Below T_C, ν_{01} slows further down to room temperature and, then, saturates in the MHz range. This relaxation is probably related to polar fluctuations in the paraelectric phase due to Nb atoms dynamics and, below T_C, due to the dynamics of the ferroelectric domains.

(iv) A relaxation, ν_{DW}, suddenly appears in the spectra below T_C, it hardens significantly on cooling, and, finally, it saturates at about 10 GHz, which is consistent with the oscillations of the ferroelectric domain walls.

The structural ferroelectric-paraelectric transition has been observed experimentally by electron diffraction, and associated with the appearance of a supplementary mirror plane perpendicular to the polar axis. At 625 K, the refined structure shows that the average structure of SBN-35 is tetragonal with an almost negligible orthorhombic distortion. The combination of structural and dielectric studies in SBN-35 suggests that ferroelectricity in TTBs in caused by a more complex mechanism than in perovskites.

ACKNOWLEDGMENTS

This work was supported by the Czech Science Foundation (Project No. 16–09142S) and by the operational program Research, Development and Education financed by European structural and investment funds and the Czech Ministry of Education, Youth and Sports (Project No. Solid21-CZ.02.1.01/0.0/0.0/16 019/0000760). E.B. wishes to thank Petr Ondrejkovič for color manipulation of the PFM figures and to Jiří Hlinka for useful discussions.

[1] R. A. Cowley, S. N. Gvasaliya, S. G. Lushnikov, B. Ressli, and G. M. Rotaru, Relaxing with relaxors: A review of relaxor ferroelectrics, Adv. Phys. **60**, 229 (2011).

[2] J. Dec, W. Kleemann, T. Woike, and R. Pankrath, Random-field Ising-type transition of pure and doped SBN from the relaxor into the ferroelectric state, Eur. Phys. B **14**, 627 (2000).

[3] A. M. Glass, Investigation of the electrical properties of $Sr_{1-x}Ba_xNb_20_6$ with special reference to pyroelectric detection, J. Appl. Phys. **40**, 4699 (1969).

[4] T. S. Chernaya, B. A. Maksimov, I. V. Verin, L. I. Ivleva, and V. I. Simonov, Crystal structure of $Ba_{0.39}Sr_{0.61}Nb_2O_6$ single crystals, Kristallografiya **42**, 421 (1997).

[5] P. B. Jamieson, S. C. Abrahams, and J. L. Bernstein, Ferroelectric tungsten bronze-type crystal structures. i. barium strontium niobate $Ba_{0.27}Sr_{0.75}Nb_2O_{5.78}$, J. Chem. Phys. **48**, 5048 (1968).

[6] M. D. Ewbanks, R. R. Neurgaonkar, and W. K. Cory, Photorefractive properties of strontium barium niobate, J. Appl. Phys. **62**, 374 (1987).

[7] J. R. Oliver, R. R. Neurgaonkar, and L. E. Cross, A thermodynamic phenomenology for ferroelectric tungsten bronze $Sr_{0.6}Ba_{0.4}Nb_2O_6$, J. Appl. Phys. **64**, 37 (1988).

[8] G. Burns, J. D. Axe, and D. F. O'Kane, Raman measurements of $NaBa_2Nb_5O_{15}$ and related ferroelectrics, Solid State Comm. **7**, 933, (1969).

[9] E. Buixaderas, M. Savinov, M. Kempa, S. Veljko, S. Kamba, J. Petzelt, R. Pankrath, and S. Kapphan, Infrared and dielectric spectroscopy of the relaxor ferroelectric $Sr_{0.61}Ba_{0.39}Nb_2O_6$, J. Phys.: Condens. Matter **17**, 653 (2005).

[10] G. H. Olsen, U. Aschauer, N. A. Spaldin, S. M. Selbach, and T. Grande, Origin of ferroelectric polarization in tetragonal tungsten-bronze-type oxides, Phys. Rev. B **93**, 180101(R) (2016).

[11] E. Buixaderas, I. Gregora, J. Hlinka, J. Dec, and T. Lukasiewicz, Raman and IR phonons in ferroelectric $Sr_{0.35}Ba_{0.69}Nb_2O_{6.04}$ single crystals, Phase Trans. **86**, 217 (2013).

[12] A. Speghini, M. Bettinelli, U. Caldiño, M. O. Ramírez, D. Jaque, L. E. Bausá, and J. García Solé, Phase transition in $Sr_xBa_{1-x}Nb_2O_6$ ferroelectric crystals probed by Raman spectroscopy, J. Phys. D: Appl. Phys. **39**, 4930 (2006).

[13] S. Shin, T. H. Kim, J.-H. Ko, S. Kojima, K.-S. Lim, and T.-Y Koo, Vibrational properties of strontium barium niobate relaxor single crystals studied by Raman spectroscopy, Ferroelectrics **488**, 1 (2015).

[14] F. Prokert, Neutron scattering studies on strontium barium niobate, Phys. Status Solidi B **113**, 239 (1982).

[15] F. M. Jiang, J. H. Ko, and S. Kojima, Central peaks and Brillouin scattering in uniaxial relaxor single crystals of $Sr_{0.61}Ba_{0.39}Nb_2O_6$, Phys. Rev. B **66**, 184301 (2002).

[16] M. S. Primrose, J. Toulouse, J. Bock, and C. Randall, Raman spectroscopy study of reduced strontium barium niobate (SBN61) and hints of supergrowth or intergrowth structures, J. Raman Spectrosc. **49**, 1849 (2018).

[17] E. Buixaderas, C. Kadlec, M. Kempa, V. Bovtun, M. Savinov, P. Bednyakov, J. Hlinka, and J. Dec, Fast polarization mechanism

in the uniaxial tungsten-bronze relaxor SBN-81, Sci. Rep. **7**, 18034 (2017).

[18] T. Lukasiewicz, M. A. Swirkowicz, J. Dec, W. Hofman, and W. Szyrski, Strontium-barium niobate single crystals, growth and ferroelectric properties, J. Cryst. Growth **310**, 1464 (2008).

[19] L. Palatinus, *L. PETS -Program for Analysis of Electron Diffraction Data* (Institute of Physics of the AS CR, Prague, Czech Republic, 2011).

[20] V. Petricek, M. Dusek, and L. Palatinus, *Jana2006 Structure Determination Software Programs* (Institute of Physics, Prague, Czech Republic).

[21] F. Prokert, J. Ihringer, and H. Ritter, X-ray diffraction study of phase transitions in $Sr_{0.39}Ba_{0.61}Nb_2O_6$ between 20 and 500 K, Ferroelectrics Lett. **20**, 73 (1995).

[22] J. Schefer, D. Schaniel, V. Pomjakushin, U. Stuhr, V. Petříček, T. Woike, M. Wöhlecke, and M. Imlau, Structural properties of $Sr_{0.61}Ba_{0.39}Nb_2O_6$ in the temperature range 10–500 K investigated by high-resolution neutron powder diffraction and specific heat measurements, Phys. Rev. B **74**, 134103 (2006).

[23] A. M. Balagurov, F. Prokert, and B. N. Savenko, Phase transition effects in the incommensurate modulated single crystal of $Sr_{0.7}Ba_{0.3}Nb_2O_6$, Phys. Status Solidi A **103**, 131 (1987).

[24] H. A. Graetsch, Large structural modulations in the relaxor ferroelectric and intermediate state of strontium rich members (x >0.6) of the $Sr_xBa_{1-x}Nb_2O_6$ (sbn) solid solution series, J. Solid State Chem. **246**, 167 (2017).

[25] J. Hlinka, J. Privratska, P. Ondrejkovic, and V. Janovec, Symmetry Guide to Ferroaxial Transitions, Phys. Rev. Lett. **116**, 177602 (2016).

[26] L. Palatinus, V. Petricek, and C. A. Correa, Acta Crystallogr. A **71**, 235 (2015).

[27] L. Palatinus, C. A. Correa, G. Steciuk, D. Jacob, P. Roussel, P. Boullay, M. Klementova, M. Gemmi, J. Kopecek, C. Domengheti, F. Camara, and V. Petricek, Acta Crystallogr. B **71**, 740 (2015).

[28] V. Shvartsman, W. Kleemann. T. Łukasiewicz, and J. Dec, Nanopolar structure in $Sr_xBa_{1-x}Nb_2O_6$ single crystals tuned by Sr/Ba ratio and investigated by piezoelectric force microscopy, Phys. Rev. B **77**, 054105 (2008).

[29] C. David, A. Tunyagi, K. Betzler, and M. Wöhlecke, Compositional dependence of optical and vibrational properties of strontium barium niobate $Sr_xBa_{1-x}Nb_2O_6$, Phys. Stat. Sol. (B) **244**, 2127 (2007).

[30] S. D. Ross, The vibrational spectra of lithium niobate, barium sodium niobate and barium sodium tantalate, J. Phys. C **3**, 1785 (1970).

[31] F. Gervais, *Infrared and Millimeter Waves*, edited by K. J. Button (Academic Press, New York, 1983), Chap. 7, p. 279.

[32] E. Buixaderas, V. Porokhonskyy, A. Pashkin, M. Savinov, and J. Petzelt, Broad-band dielectric spectroscopy of $Ba_2NaNb_5O_{15}$ single crystal, Eur. Phys. J. B **30**319 (2002).

[33] E. L. Venturini, E. G. Spencer, P. V. Lenzo, and A. A. Ballman, Refractive Indices of Strontium Barium Niobate, J. Appl. Phys. **39**, 343 (1968).

[34] M. Pasciak, M. Kopecky, J. Kub, J. Fabry, J. Dec, P. Ondrejkovic, J. Hlinka, and E. Buixaderas, X-ray diffuse scattering observations for $Sr_xBa_{1-x}Nb_2O_6$ single crystals with $x =$ 0.35 and 0.81, Phase Trans. **91**, 969 (2018).

[35] M. Aftabuzzaman, M. A. Helal, R. Paszkowski, J. Dec, W. Kleemann, and S. Kojima, Electric field and aging effects of uniaxial ferroelectrics $Sr_xBa_{1-x}Nb_2O_6$ probed by Brillouin scattering, Sci. Rep. **7**, 11615 (2017).

[36] E. Buixaderas, P. Bérešová, P. Ondrejkovič, P. Vaněk, M. Savinov, P. Bednyakov, J. Dec, D. Mareš, M. Ševčík, and M. Landa, Acoustic phonons in unfilled tetragonal tungsten-bronze crystals, Phase Trans. **91**, 976 (2018).

[37] E. Buixaderas, V. Bovtun, M. Kempa, D. Nuzhnyy, M. Savinov, P. Vanek, I. Gregora, and B. Malic, Lattice dynamics and domain wall oscillations of morphotropic Pb(Zr, Ti)O_3 ceramics, Phys Rev. B **94**, 054315 (2016).

[38] G. Arlt, Ferroelastic domain walls as powerful shear wave emitters at microwaves, Ferroelectrics **172**, 95 (1995).

[39] J. Dec, W. Kleemann, V. V. Shvartsman, D. C. Lupascu, and T. Lukasiewicz, From mesoscopic to global polar order in the uniaxial relaxor ferroelectric $Sr_{0.8}Ba_{0.2}Nb_2O_6$, Appl. Phys. Lett **100**, 052903 (2012).

[40] P. Ondrejkovic, M. Kempa, J. Kulda, B. Frick, M. Appel, J. Combet, J. Dec, T. Lukasiewicz, and J. Hlinka, Dynamics of Nanoscale Polarization Fluctuations in a Uniaxial Relaxor, Phys. Rev. Lett. **113**, 167601 (2014).